# Impact of 2-D Bubble Dynamics on the Selectivity of Fast Gas–Liquid Reactions

**Johannes G. Khinast**
Dept. of Chemical and Biochemical Engineering, Rutgers University, Piscataway, NJ 08854

*The impact of mass transfer and bubble-wake dynamics on the selectivity of fast gas–liquid reactions was studied for a parallel-consecutive reaction network using numerical simulations. Depending on bubble size and shape, the bubble wake can be closed or open. Spherical bubbles have only closed wakes without recirculation, while all other bubble types can exhibit recirculation or vortex shedding depending on their shape and the Reynolds number. Although the importance of local mixing on the selectivity of complex reactions was studied by many research groups, there exist no studies addressing the effect of local mixing patterns (bubble-wake dynamics) close to single bubbles on fast gas–liquid reactions, that is, reactions that occur close to the gas–liquid interface. To study this class of reactions, a 2-D bubble model was developed, which accounts for liquid flow around the bubble, mass transfer, and reactions. It was found that different residence times in the bubble wake and at the bubble roof can lead to the formation of different products; recirculation in the bubble wake acts as a transport barrier for the liquid-phase reactants; and vortex shedding causes a qualitatively different mixing pattern than that of a closed wake, leading to a different product distribution in the case of mixing-sensitive reactions. Since bubble shapes and sizes can be controlled by changing operating conditions or design parameters, this analysis can be applied to actual reaction systems to enable a rational design, control, scale-up, and optimization of existing and new processes.*

## Introduction

Bubble (slurry) reactors are used extensively to carry out a variety of gas–liquid and gas–liquid–solid reactions. Classic examples are hydrogenations, liquid-phase oxidations, hydroformylations, carbonylations, Fisher-Tropsch synthesis, industrial fermentations, or bioremediations (Ramachandran and Chaudhari, 1983; Mills and Chaudhari, 1999). The engineering of these reactors has been reviewed in books by Shah (1979), Ramachandran and Chaudhari (1983), Gianetto and Silveston (1986), Fan (1989), and articles by Beenackers and van Swaaij (1986) and Krishna and Ellenberger (1995). One of the disadvantages of this reactor type is the strong liquid back mixing, and more generally, the complexity of the hydrodynamics and the lack of understanding of its impact on the yield and selectivity of multiple reactions.

During bubble-column operation gas is sparged at the bottom of the column, and the resulting buoyancy-driven flow causes circulation and gas–liquid mixing. In bubble-slurry reactors, a solid phase (catalyst) is suspended by the vigorous mixing induced by the rising bubbles. Depending on the operating and design parameters (superficial gas velocity, column diameter, pressure, liquid viscosity, surface tension, catalyst loading, and so on), different flow regimes can be obtained in the reactor. At low superficial gas velocities bubbles are rising in straight paths with minimal interaction or coalescence. This is called the *dispersed* or *bubbly flow-regime*. At intermediate gas velocities a meandering *vortical-spiral flow* develops (Mudde et al., 1997a,b), and at high velocities a *churn-turbulent flow* develops, which is characterized by bubble coalescence, breakup, and vigorous mixing. A bimodal distribution of bubble sizes becomes clearly evident in this regime (Krishna et al., 1999). Depending on the system parameters, there may be additional regimes with different characteristics (Lin et al., 1996; Hyndman et al., 1997; Reese and Fan, 1997). Clearly, each flow regime has signifi-

cantly different mass-transfer and liquid-mixing characteristics, and therefore influences selectivity and yield of mixing-sensitive reactions (Khinast et al., 1999a,b).

Low yield and selectivity of a process result in the formation of large quantities of byproducts requiring separation, disposal, or rework. Thus, high yield and selectivity are critical for the competitiveness of a process and for minimizing environmental impact. The importance of mixing and segregation for chemical reactions was first studied for homogeneous systems in the 1950s by van Krevelen (1958), Kramers (1958), and Danckwerts (1958). Impact of stirring on the selectivity of parallel or consecutive reaction networks in a homogenous system was investigation by Paul and Treybal (1971) (iodine and L-tyrosine), Bourne et al. (1977) (bromination of resorcin), Nienow et al. (1992) (diazo-coupling), Villermaux et al. (1992) (iodate/iodine reactions), and other research groups. Similar concepts apply to multiphase systems, and a substantial body of knowledge has been built up in this field (Doraiswamy and Sharma, 1984; Baldyga and Bourne, 1999). In the last years it was found that even enantio- and stereoselectivity can be influenced by mixing and mass transfer. Sun et al. (1996) showed that the local concentration of dissolved hydrogen is the main variable determining the enantioselectivity in the hydrogenation of ethyl pyrovate to (*R*)- and (*S*)-ethyl lactate over chinchona-alkoid-modified Pt. An increase of the mass-transfer coefficient improved the enantioselectivity to (*R*)-ethyl lactate by a factor of 3 (!). Similar results were observed for the asymmetric hydrogenation of geraniol over binap-Ru(II) (Sun et al., 1997). Impact of mixing on autocatalytic and biological systems was reviewed by Epstein (1995).

In the case of slow reactions the large-scale features of the flow, that is, macromixing, determine selectivity and yield. Computational fluid dynamics (CFD) codes can be used to simulate macromixing characteristics. However, in the case of fast or instantaneous reactions, microscale flow structures, down to the Kolmogoroff and Batchelor scale, become important, and an accurate prediction of the reactor performance requires models for both the macro- and microscale. In the chemical engineering research community much work has been devoted to developing multiscale models that account both for macro- and micromixing (Sundaresan, 2000). For example, micromixing models, like the Interaction-by-Exchange-with-the-Mean and related models (David and Villermaux, 1987; Villermaux and Falk, 1994) were recently combined with CFD models (Fox. 1998) to predict the performance of fast reactions in stirred-tank reactors.

Although much progress has been made in this area, more research is needed. Especially with regard to fast multiphase reactions, our understanding is still limited, mostly because current turbulence models cannot describe the small-scale features of multiphase flows. For example, fast gas–liquid reactions take place close to the gas–liquid interface, that is, in case of bubbles, both at the bubble roof and in the wake region. For this class of reactions, micromixing close to individual bubbles will determine selectivity and yield of fast reactions and micromixing models have to take into account the local flow patterns around individual bubbles. If the reaction is heterogeneously catalyzed, the local density of the catalyst close to the bubble is important. In a study on the motion of solid particles in the wake behind a solid 2-D cylinder, Froncioni et al. (1997) found that particles with different Stokes numbers accumulated in different regions of the wake. Thus, for fast gas–liquid–solid reactions, the liquid and particle flow close to individual bubbles determines the reactor performance. In the literature only simplified models of reacting bubbles were presented (Fan and Tsuchiya, 1990; Kleinman and Reed, 1995; Long and Kalachev, 2000). Therefore, to the best of our knowledge, this study addresses for the first time the impact of bubble dynamics on the selectivity of fast gas–liquid reactions.

In real multiphase systems a large number of bubbles rise in the liquid. Conceptually, the behavior of single bubbles and bubble swarms is quite different. In a reactor, bubbles have different diameters, and it is hard to predict a size distribution, especially in the presence of coalescence and breakup. Different-sized bubbles have different terminal velocities and tend to follow other bubble's trails. Although in practice bubble–bubble interactions are important, they will be ignored in this article, in which we will primarily focus on reactions close to single bubbles, since we expect that a single-bubble model will capture most of the effects in terms of reaction yield and selectivity. The interaction with other bubbles, that is, the bubble swarm dynamics, will be addressed later. Therefore, the results of this study apply mainly to the bubbly and vortical-spiral flow regime, where bubble–bubble interactions are of less importance.

For many practical systems operated in the bubbly or vortical-spiral flow regime, the bubble size is small, and depending on the viscosity and surface tension, the bubble shapes are spherical or elliptical. Therefore, this study is intended to determine qualitative differences between these two bubble types in terms of their reactivity. A simplification of the presented study is the use of a 2-D bubble model. Although it is well known that wake dynamics and vortex shedding of 2-D and 3-D bubbles differ significantly, it can be assumed that the impact of the wake dynamics on the reaction selectivity and local mixing is similar.

This article is organized as follows: the next section provides background information on single bubble dynamics; the third section introduces the bubble model that was used in this study; in the fourth section a numerical method and model verification are presented, followed by the results of this work in section five.

## Background

Shapes and sizes of single rising bubbles were investigated by Haberman and Morton (1953), among others. They found that bubble shape and rise velocity depend mainly on viscosity, gravity, density, bubble size, surface tension, and pressure. (One should in fact include other quantities such as fluid purity, surfactant concentration, and fluid turbulence.) Based on these parameters, dimensionless numbers can be formed to correlate experimental results. The most common are the *Eötvös* or *Bond* number, $Eo = g\,\rho_l d_b^2/\sigma$ (= ratio of gravity to surface tension; when small, surface tension dominates over the hydrostatic pressure difference from top to bubble rear and the bubble remains spherical), the *Morton* number, $Mo = g\,\mu_l^4/(\rho_l \cdot \sigma^3)$ (= ratio of viscous forces to surface tension, that is, the tendency of viscous forces to drag the bubble's lateral border backward in a spherical cap), and the bubble

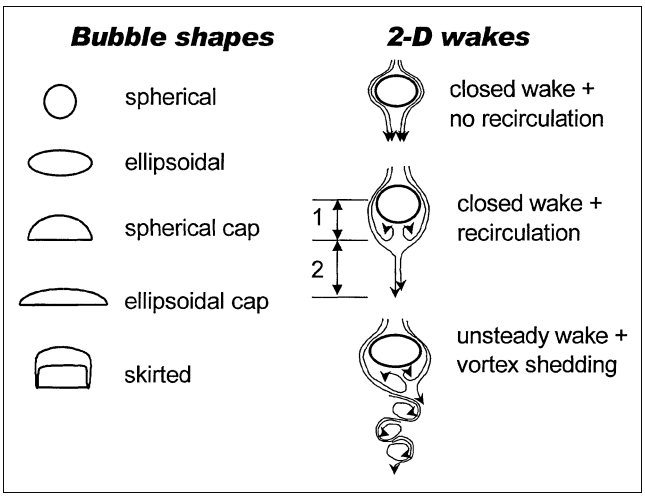


**Figure 1. Different bubble shapes and wake structures of a single bubble rising in a stagnant liquid.**

1 = primary wake; 2 = secondary wake [After Fan and Tsuchiya (1990)].

*Reynolds* number based on terminal rise velocity, $R_b = d_b U_\infty \rho_l / \mu_l$ (= ratio of the interia to viscous forces). Depending on these numbers, the shape of a bubble can be spherical, ellipsoidal, ellipsoidal cap, or spherical cap (Fan and Tsuchiya, 1990), as shown in Figure 1. In some highly viscous liquids, the formation of skirts, that is, thin annular films of gas trailing behind the rim of a large spherical-cap bubble, is observed (Bhaga and Weber, 1981). Under certain conditions, bubble shape oscillations occur (Fan and Tsuchiya, 1990). Correlations for single-bubble rise velocities in liquids and liquid–solid suspensions were reported by Grace et al. (1976), Miyahara and Takahashi (1985), Jean and Fan (1990), and others. For low to intermediate Eötvös numbers, typically spherical or ellipsoidal bubbles are obtained, which are the types of bubbles that are most frequently found in bubble columns in the bubbly or vortical-spiral flow regime. The lower limit of the aspect ratio $\delta$ of ellipsoidal bubbles (bubble height over width) is 0.25, and in most cases $\delta$ is larger than 0.4 (Fan and Tsuchiya, 1990).

The most important feature in terms of local mixing is the dynamic behavior of the bubble wake, which was extensively studied by Fan's group (Fan and Tsuchiya (1990). The wake consists of a primary wake moving in close association with the bubble, and a secondary wake extending far downstream (Wu, 1986). The specific details of the wake structures, especially in 3-D, are not easy due to the varying flow instabilities occurring over a wide range of Reynolds numbers (Fan and Tsuchiya, 1990). For gas bubbles, typically three different wake types are observed, as shown in Figure 1: (1) a steady wake without circulation; (2) a steady wake with well-developed circulation; and (3) an unsteady wake with vortical structures and vortex shedding (Lindt, 1971, 1972; Hills, 1975; Bhaga and Weber, 1981; Saffman, 1986; Miyahara et al., 1988). High Reynolds numbers, which lead to strongly turbulent wakes (as seen behind solid bodies), are rarely observed, since they lead to bubble breakup (Fan and Tsuchiya, 1990). From Figure 1 it is obvious that different wake types exhibit entirely different mixing properties.

The development of recirculating wakes behind bubbles was extensively discussed by Ryskin and Leal (1984a,b) and Leal (1989). At solid boundaries vorticity is generated due to the no-slip boundary condition. Vorticity is then transported throughout the fluid by convection and diffusion and may be enhanced by vortex stretching. At bubble interfaces, however, the situation is fundamentally different, since the tangential stresses are approximately zero, that is, the so-called "perfect-slip" condition holds. (In fact, very small bubbles in unpurified liquids behave like solid particles, that is, there is no recirculation inside the bubble due to a surface-tension gradient caused by impurities, which accumulate at the bubble rear.) Moore (1958) pointed out that at a perfect-slip boundary, vorticity is created inversely proportional to the curvature. In spherical bubbles vorticity formation is not sufficient to create a recirculating wake or vortex shedding, but in the case of elliptical or spherical-cap bubbles the increasing curvature creates sufficient vorticity to cause recirculation or the shedding of vortices. Therefore, onset of recirculation and vortex shedding is determined by the aspect ratio. Bubbles with a smaller aspect ratio show recirculation and vortex shedding at lower Reynolds numbers.

A significant amount of work was devoted to understanding mass transfer from a single rising bubble into a liquid, for example, by Baird and Davidson (1962), Calderbank et al. (1970), Brignell (1974), Weber (1975), Coppus and Rietma (1980, 1981), Nguyen-Tien et al. (1985), Arters and Fan (1990), Song and Fan (1990), and recently by Ponoth and McLaughlin (2000).

Since bubble size and shape can be adjusted by changing sparger design, nozzle size, operating pressure, gas feed rate, liquid viscosity (additives like carboxymethyl cellulose, HEC, PEPPG), and surface tension (surfactants), byproduct formation of fast gas–liquid reactions can be controlled, if indeed bubble-wake dynamics impact yield and selectivity. In order to investigate this hypothesis, a bubble model was developed, which is presented in the next section.

## Problem Formulation

The bubble is assumed to be a stationary object immersed in a liquid that is flowing past the bubble at terminal velocity. Shape and orientation of the bubble remain constant, representing a bubble rising in a straight path. It is known that vortex shedding causes bubbles to rise in a rocking motion with a zigzag or spiraling path. However, the assumption of constant shape and orientation is reasonable, since the main focus of this work is not the accurate description of the bubble hydrodynamics but the qualitative impact of bubble-wake dynamics on the reaction selectivity. Thus, bubble-wake dynamics and vortex shedding behind a rising bubble and a stationary object with perfect-slip boundary condition can be assumed to be similar in terms of the local mixing behavior. Other assumptions are negligible surface-tension gradients, isothermal flow, and the absence of bubble–bubble interactions. Finally, it is assumed that the flow is laminar, which is typically true below Reynolds numbers of 200 (Fan and Tsuchiya 1995).

The model used in this study is an unstationary, cylindrical 2-D model. A spherical bubble model, where the assumption of axisymmetric flow reduces the 3-D to a 2-D model, is not

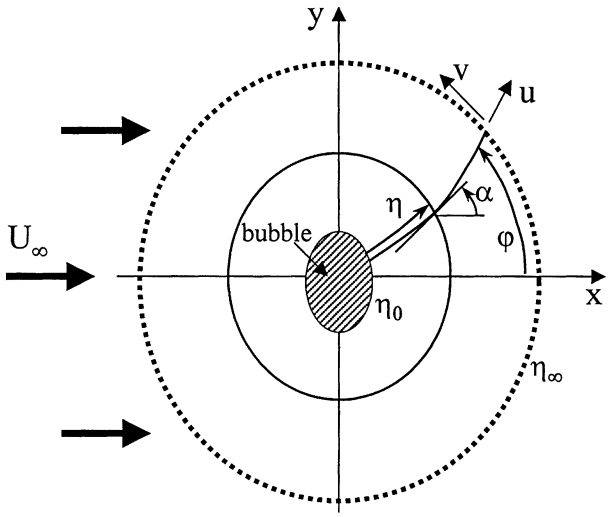


**Figure 2. Elliptical coordinate system used in the simulations.**

applicable in this case, since the effects of asymmetric wakes (vortex shedding) on the reaction selectivity are to be examined. Clearly, the flow around a bubble in a bubble column is inherently 3-D, and 2-D vortex shedding is different from the 3-D one. However, the mechanisms are related to each other, and with respect to reactive mixing the behavior can be expected to be similar. Only circular and elliptical bubbles will be studied, since the wake dynamics of elliptical bubbles and circular- (or elliptical-) cap bubbles are rather similar. The main qualitative difference is expected to occur between bubbles that cause or do not cause recirculation and/or shedding (that is, elliptical and circular bubbles). Bubble aspect ratios of 1, 0.5 (and 0.25) are studied at Reynolds numbers between 1 and 100.

The governing equations for the unsteady flow of an incompressible fluid around a rising bubble are the continuity and Navier-Stokes equations. Due to the elliptical nature of the problem, the model equations can be transformed into an elliptical coordinate system (Figure 2) with the coordinate direction $\eta$ and $\varphi$ given by the transformation:

$$x = a \sinh \eta \cdot \cos \varphi$$

$$y = a \cosh \eta \cdot \sin \varphi. \tag{1}$$

2a is the interfocal distance of the elliptical bubble, that is, $a = \sqrt{d_1^2 - d_2^2}$ , where $d_1 = a \cosh \eta_0$ (the major semiaxis of the ellipse), $d_2 = a \sinh \eta_0$ (the minor semiaxis of the ellipse), and $\eta_0 = \ln \sqrt{(1+\delta)/(1-\delta)}$ , with $\delta$ being the aspect ratio $d_2/d_1 < 1$. Here $\eta$ ranges from $\eta_0$ to $\infty$, and $\varphi$ from 0 to $2\pi$. Both coordinates are dimensionless.

The relation between physical and transformed coordinate systems can be described by the metric tensor $\boldsymbol{g}$, which relates the contributions of a small distance $\Delta s$ to small changes in the transformed coordinates (Fletcher, 1987). If the coordinate system is orthogonal, that is, the angle between coordinate lines is 90°, the metric tensor contains only diagonal terms, which are given by

$$g_{ii} = \left(\frac{\partial x}{\partial u_i}\right)^2 + \left(\frac{\partial y}{\partial u_i}\right)^2, \tag{2}$$

where $x$ and $y$ are the physical coordinates, and $u_i$ are the transformed coordinates, that is, ($\eta$, $\varphi$). It is, convenient to define scale factors $H_i$

$$H_i = \sqrt{g_{ii}}. \tag{3}$$

For our coordinate system

$$H_1 = H_2 = a\sqrt{\cosh^2 \eta - \sin^2 \varphi}. \tag{4}$$

The coordinate system satisfies the orthogonality condition, $x_\eta x_\varphi + y_\eta y_\varphi = 0$. The grid aspect ratio, which is defined as the ratio of the magnitudes of the grid tangent vectors for $\Delta\eta = \Delta\varphi$, is given by

$$AR = \frac{H_2}{H_1} = 1. \tag{5}$$

Thus, the grid is conformal (that is, it satisfies the Cauchy-Riemann condition), which further simplifies the equations. The physical orientation of the computational grid (tangent to the $\eta$-coordinate lines) relative to the $x$-axis is given by the direction cosine (see Figure 2):

$$\cos \alpha = \frac{x_\eta}{H_1} = \frac{\cosh \eta \cos \varphi}{\sqrt{\cosh^2 \eta - \sin^2 \varphi}}. \tag{6}$$

In order to make the governing equations dimensionless, $a$ ( = half the interfocal distance) is used as characteristic length and the terminal rise velocity as the reference velocity $U_\infty$, resulting in the dimensionless variables.

$$t = \frac{\hat{t} U_\infty}{a}, \qquad P = \frac{\hat{P}}{U_\infty^2 \rho}, \quad u = \frac{\hat{u}}{U_\infty}, \quad v = \frac{\hat{v}}{U_\infty}, \tag{7}$$

where $u$ and $v$ are the two dimensionless velocities in the $\eta$- and $\varphi$-directions. The Reynolds number $\hat{R}$ is

$$\hat{R} = \frac{a U_\infty \rho}{\mu}. \tag{8}$$

The Reynolds number used in this article is the Reynolds number, $R$, based on the major axis of the ellipse. Thus, $R$ is related to $\hat{R}$ by

$$R = 2 \cosh \eta_0 \hat{R}. \tag{9}$$

In many studies, the equivalent bubble diameter is used to obtain the bubble Reynolds number $R_b$. However, this would

lead to very small Reynolds numbers for low aspect ratios (a flat plate of length $2 \cdot d_1$ would lead to zero equivalent diameter). The bubble Reynolds number $R_b$ based on the equivalent diameter is given by

$$R_b = \sqrt{\delta}\, R = 2 \cosh \eta_0 \sqrt{\delta}\, \hat{R}. \tag{10}$$

The continuity and Navier-Stokes equations in a 2-D conformal, orthogonal coordinate systems are

$$\frac{\partial (h\, u)}{\partial \eta} + \frac{\partial (h\upsilon)}{\partial \varphi} = 0 \tag{11}$$

$$\frac{\partial u}{\partial t} + \frac{u}{h}\frac{\partial u}{\partial \eta} + \frac{\upsilon}{h}\frac{\partial u}{\partial \varphi} - \frac{\upsilon^2}{h^2} h_\eta + \frac{u\upsilon}{h^2} h_\varphi = -\frac{1}{h}\frac{\partial P}{\partial \eta} + \frac{1}{\hat{R} \cdot h}\left( \frac{\partial}{\partial \eta}\left( \frac{1}{h^2}\frac{\partial hu}{\partial \eta} \right) + \frac{\partial}{\partial \varphi}\left( \frac{1}{h^2}\frac{\partial hu}{\partial \varphi} \right) - \frac{2}{h^3}\left( h_\eta \frac{\partial h\upsilon}{\partial \varphi} - h_\varphi \frac{\partial h\upsilon}{\partial \eta} \right) \right) \tag{12}$$

$$\frac{\partial \upsilon}{\partial t} + \frac{u}{h}\frac{\partial \upsilon}{\partial \eta} + \frac{\upsilon}{h}\frac{\partial \upsilon}{\partial \varphi} + \frac{u\upsilon}{h^2} h_\eta - \frac{u^2}{h^2} h_\varphi = -\frac{1}{h}\frac{\partial P}{\partial \varphi} + \frac{1}{\hat{R} \cdot h}\left( \frac{\partial}{\partial \eta}\left( \frac{1}{h^2}\frac{\partial h\upsilon}{\partial \eta} \right) + \frac{\partial}{\partial \varphi}\left( \frac{1}{h^2}\frac{\partial h\upsilon}{\partial \varphi} \right) - \frac{2}{h^3}\left( h_\varphi \frac{\partial hu}{\partial \eta} - h_\eta \frac{\partial hu}{\partial \varphi} \right) \right), \tag{13}$$

where

$$h = \frac{H}{a} = \sqrt{\cosh^2 \eta - \sin^2 \varphi}, \qquad h_\eta = \frac{\partial h}{\partial \eta} = \frac{\sinh \eta \cosh \eta}{h},$$

$$h_\varphi = \frac{\partial h}{\partial \varphi} = -\frac{\sin \cos \varphi}{h}. \tag{14}$$

The dimensionless stress tensor is given by (Tannehill et al., 1997):

$$\boldsymbol{\tau} = \frac{\hat{\boldsymbol{\tau}}}{U_t^2 p} \begin{pmatrix} -p + \frac{2}{\hat{R}}\left( \frac{1}{h}\frac{\partial u}{\partial \eta} + \frac{\upsilon}{h^2} h_\varphi \right) & \frac{1}{\hat{R}}\left( \frac{\partial (\upsilon/h)}{\partial \eta} + \frac{\partial (u/h)}{\partial \varphi} \right) \\ \frac{1}{\hat{R}}\left( \frac{\partial (\upsilon/h)}{\partial \eta} + \frac{\partial (u/h)}{\partial \varphi} \right) & -P + \frac{2}{\hat{R}}\left( \frac{1}{h}\frac{\partial \upsilon}{\partial \varphi} + \frac{u}{h^2} h_\eta \right) \end{pmatrix}. \tag{15}$$

The boundary conditions at the bubble–liquid interface are those of impermeability and perfect slip, that is,

$$u = 0 \qquad \text{and} \qquad \frac{\partial \upsilon}{\partial \eta} = \frac{h_\eta}{h}\upsilon. \tag{16}$$

For verification of the numerical method, the flow around a solid cylinder is chosen. In this case, the no-slip boundary condition will be used, that is, the second part of the boundary condition in Eq. 16 is replaced by $\upsilon = 0$.

In the physical domain the flow is not confined. Nevertheless, a fictional external boundary is needed at a certain distance from the bubble. The necessary distance to minimize blockage effects due to this "artificial boundary condition" are approximately twenty bubble diameters (see the fourth section). As the inflow boundary condition the velocity of the uniform flow is chosen, that is,

$$u = \cos \alpha, \qquad \upsilon = -\sin \alpha. \tag{17}$$

In the outflow region, a smooth linear transition with respect to $\varphi$ between the Dirichlet boundary conditions, Eq. 17, and Neumann boundary conditions is chosen,

$$\text{at } \eta = \eta_\infty\text{:} \quad \frac{\partial u}{\partial \eta} = 0, \qquad \frac{\partial \upsilon}{\partial \eta} = 0. \tag{18}$$

Hence, the boundary conditions at infinity are those of uniform flow outside the wake and those of zero derivative inside the wake.

In the model four reactive species, $A$, $B$, $R$, and $S$ are considered. Species $A$ is a liquid reactant, $B$ the dissolved gaseous reactant, and $R$ and $S$ are the two products. The mass balances for the reactive species in an inert solvent in dimensionless form are

$$\frac{\partial c_i}{\partial t} + \frac{1}{h}\left( u\frac{\partial c_i}{\partial \eta} + \upsilon \frac{\partial c_i}{\partial \varphi} \right) = \frac{1}{Pe_i h^2}\left( \frac{\partial^2 c_i}{\partial \eta^2} + \frac{\partial^2 c_i}{\partial \varphi^2} \right) + \sum_{j=1}^{m} \nu_{ij} r_j(c_i), \qquad i = A, B, R, S, \tag{19}$$

where the dimensionless concentrations are defined as

$$c_i = \frac{\hat{c}_i}{c_{A,in}}. \tag{20}$$

The Peclet number of every component is

$$Pe_i = \frac{U_\infty a}{D_i} = \hat{R} \cdot Sc_i, \tag{21}$$

where $Sc_i$ is the Schmidt number of species $i$. The network investigated is a parallel $(B)-$consecutive $(R)$ reaction network, which is frequently found in reactions of industrial importance, that is,

$$R_1\text{:} A + B \rightarrow R$$
$$R_2\text{:} R + B \rightarrow S, \tag{22}$$

with dimensionless reaction rates

$$r_1 = Da_1 \cdot c_A \cdot c_B, \qquad r_2 = Da_2 \cdot c_R \cdot c_B. \tag{23}$$

The Damköhler numbers are defined as

$$Da_1 = \frac{a \cdot k_1 \cdot c_{A,in}}{U_\infty}, \qquad Da_2 = \frac{a \cdot k_2 \cdot c_{A,in}}{U_\infty}. \tag{24}$$

The ratio between $Da_2$ and $Da_1$ is $\kappa$, that is, $\kappa = Da_2/Da_1$. The boundary conditions at the bubble surface are

$$\left.\frac{\partial c_A}{\partial \eta}\right|_{\eta=\eta_0} = \left.\frac{\partial c_R}{\partial \eta}\right|_{\eta=\eta_0} = \left.\frac{\partial c_S}{\partial \eta}\right|_{\eta=\eta_0} = 0,$$

$$c_B|_{\eta=\eta_0} = \hat{c}_{B,\mathrm{eq}}/c_{A,in} = c_{B,\mathrm{eq}}, \tag{25}$$

that is, the concentration of the gaseous reactant at the bubble surface is assumed to be equal to the equilibrium concentration for a constant partial pressure in the bubble (pure gas). The boundary conditions at infinity are similar to the ones of the momentum balance. The inflow boundary conditions are

$$c_A|_{\eta=\eta_\infty} = 1, \qquad c_B|_{\eta=\eta_\infty} = c_R|_{\eta=\eta_\infty} = c_S|_{\eta=\eta_\infty} = 0. \tag{26}$$

The outflow boundary conditions are again a linear transition (with respect to $\varphi$) between Dirichlet (Eq. 26) and Neumann boundary conditions

$$\left.\frac{\partial c_A}{\partial \eta}\right|_{\eta=\eta_\infty} = \left.\frac{\partial c_B}{\partial \eta}\right|_{\eta=\eta_\infty} = \left.\frac{\partial c_R}{\partial \eta}\right|_{\eta=\eta_\infty} = \left.\frac{\partial c_S}{\partial \eta}\right|_{\eta=\eta_\infty} = 0. \tag{27}$$

The set of parameters used in the calculation is reported in Table 1 and are typical for gas–liquid reactions at elevated temperatures and pressures. The bubble types studied are elliptical and circular bubbles. For a circular bubble a $\delta$-value of 0.98 was used to approximate the geometry ($\delta = 1$ would lead to a singular grid). Note that since it is assumed that the bubble consists of a pure gas (such as hydrogen), no depletion occurs and $\hat{c}_{B,eq}$ remains constant. Additionally, it is assumed that the bubble diameter remains constant during the reaction, which is a good approximation for many industrial systems.

## Numerical Method and Model Verification

### *Numerical solution*

The method used to solve the model equations is based on a finite difference, staggered-grid discretization of the spatial derivatives in the Navier-Stokes (NSE) and continuity (CE) equation and a finite-volume discretization of the mass balances to guarantee mass conservation (Fletcher, 1997). The chosen grid is nonuniform. A different grid for mass and momentum balances can be used, depending on the magnitude of velocity and concentration gradients. The Peclet numbers in the mass balances are on the order of $10^4$, leading to oscillation in the liquid-phase concentrations. Thus, a mixed scheme of donor-cell discretization ($\gamma = 1$) and central differences ($\gamma = 0$) was used. In the simulations, a value of $\gamma = 0.2$ was necessary. Donor-cell discretization was not necessary in the NSE equation up to Reynolds numbers of 200. The resulting set of differential-algebraic equations (DAE) was integrated in time using the new version of LIMEX (Deuflhard et al., 1987; Ehrig et al., 1999). This solver is based on the extrapolation of a semi-implicit Euler discretization. A major advantage of the semi-implicit discretization is that the solver is less sensitive to inconsistencies in the initial conditions.

It is well known that full spatial discretization of the Navier-Stokes equation leads to an *Index 2* DAE system. The most frequently used definition of the index of a DAE system is the minimum number of times that all or parts of the system have to be differentiated with respect to the independent variable ($t$) in order to determine derivatives of the dependent variables ($\mathbf{y}$) as a continuous function of $\mathbf{y}$ and $t$ (Brenan et al., 1996). Differentiation of the spatially discretized continuity equation does not yield time derivatives of the pressure, and therefore the resulting system is not of Index 1. Most differential-algebraic solvers are not designed for problems with index larger than 1 (DASSL, DSL48S, LIMEX). Therefore, significant efforts were devoted to develop efficient algorithms for automated index reduction of DAEs, for example, by Chowdhry and Linninger (1999). However, it was recently shown that both LIMEX and DASSL can solve Index 2 problems under certain conditions. Therefore, LIMEX was tested and we found that LIMEX can indeed solve the discretized NSE and CE. Although the system is a DAE system, we used an extrapolation level of 7 (there is no proof that convergence can be obtained for levels higher than 5), giving the fastest convergence. The Harwell sparse-matrix solver MA28 was used for the linear algebra. The resulting code was very fast and stable, and memory requirements remain moderate, implementation is straightforward, and the numerical drift of the code is negligible. The relative tolerance for LIMEX was chosen to be $0.5 \times 10^{-4}$. Only negligible differences were detected compared to solutions at a smaller relative tolerance $1 \times 10^{-6}$. However, the CPU-time was drastically increased. For the reported values, every simulation took less than 10 min on a DEC-Alpha XP 1000 for the full set of variables (4 species $+ u$, $v$, and $P$ on a $60 \times 60$ grid). The resulting number of unknowns was $7 \times 61 \times 60 = 24{,}620$).

**Table 1. Parameters Used in Calculations**

| Parameter | Value |
|---|---|
| $\hat{c}_{B,\mathrm{eq}}$ | 0.1 $c_{A,\mathrm{In}}$ |
| $\delta$ | (0.25), 0.5, 0.98 |
| $Da_1$ | 0.01, 0.1, 1 |
| $\kappa$ | 1, 20, 500 |
| $\mathrm{Sc}_A$, $Sc_R$ $Sc_S$, ($Sc_B$) | 50 (10) |

### *Drag and lift coefficient*

The drag and lift coefficients are based on the major axis of the ellipse, $2 \cdot d_1$,

$$C_l = \frac{\text{lift force}}{\frac{1}{2}\rho U_\infty^2 2 d_1}, \qquad C_d = \frac{\text{drag force}}{\frac{1}{2}\rho U_\infty^2 2 d_1}. \tag{28}$$

Thus, the lift and drag coefficients are

$$C_l = \frac{2}{R}\int_0^{2\pi} \tau_{\eta\varphi}(\eta_0,\varphi)\cos\alpha\cdot h(\eta_0,\varphi)\,d\varphi + \frac{1}{\cosh\eta_0}\int_0^{2\pi} \tau_{\eta\eta}(\eta_0,\varphi)\cdot\sin\alpha\cdot h(\eta_0,\varphi)\,d\varphi \quad (29)$$

$$C_d = -\frac{2}{R}\int_0^{2\pi} \tau_{\eta\varphi}(\eta_0,\varphi)\sin\alpha\cdot h(\eta_0,\varphi)\,d\varphi + \frac{1}{\cosh\eta_0}\int_0^{2\pi} \tau_{\eta\eta}(\eta_0,\varphi)\cos\alpha\cdot h(\eta_0,\varphi)\,d\varphi. \quad (30)$$

In Eqs. 29 and 30 the first term is the contribution due to shear stresses (= zero in case of the perfect-slip boundary condition). The second term is the contribution due to normal stress, which is equal to $(-P)$ for the no-slip boundary condition. For perfect slip, the viscous contribution to the normal stress is nonzero.

### *Accuracy and grid*

The accuracy of the presented method was evaluated by solving a test problem, for which the solution is available in the literature. The drag coefficient at low Reynolds number flows around a circular solid cylinder was chosen, since values were published in numerous experimental and numerical studies. Clift et al. (1987) reported a correlation of a large number of experimental data analyzed by Pruppacher et al. (1970):

$$c_D = 9.689R^{-0.78}(1+0.147R^{0.82}) \qquad (0.1 < R \le 5)$$
$$c_D = 9.689R^{-0.78}(1+0.227R^{0.55}) \qquad (5 < R \le 40)$$
$$c_D = 9.689R^{-0.78}(1+0.0838R^{0.82}) \qquad (40 < R \le 400). \quad (31)$$

The junctions between the curves correspond to the changes in the flow patterns, that is, closed wake without recirculation, closed wake with recirculation, and open wake with vortex shedding (Panton, 1996). For example, for $R = 20$ the predicted drag coefficient is 2.04.

First, the grid-dependence of the solution was studied. The grid was divided in equal distances in the $\eta$-direction, which leads to a finer grid close to the bubble surface in physical coordinate space. In order to resolve the concentration boundary layer (in liquids $Sc \gg 1$), a grid with even finer resolution close to the bubble was chosen (parabolic distribution in $\eta$-space). In the $\varphi$-direction grid points were positioned (between $\varphi = 0,\ \pi$), according to

$$\varphi_j = \pi\cdot\left(\frac{j-1}{m/2}\right)^{1.5} \qquad j = 1,\ m/2, \quad (32)$$

**Table 2. Computed Drag Coefficient at $R = 20$ for Different Grid Parameters***

| | $\lambda = 10$ | $\lambda = 20$ | $\lambda = 30$ | $\lambda = 40$ | $\lambda = 50$ |
|---|---|---|---|---|---|
| $n\times m = 50\times 60$ | 2.447 | 2.199 | 2.109 | 2.062 | 2.043 |
| $n\times m = 100\times 60$ | 2.505 | 2.202 | 2.110 | 2.065 | 2.051 |

*The exact value is $C_d = 2.04$.

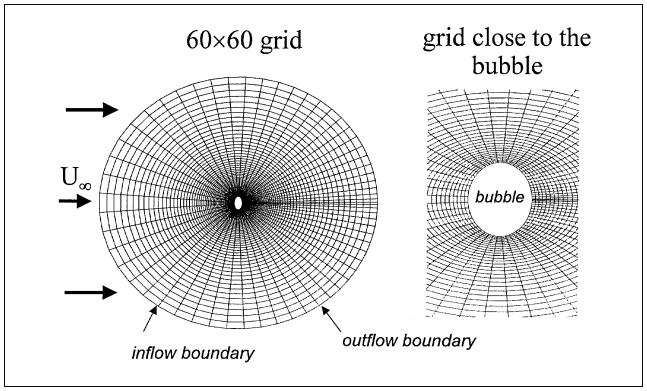


**Figure 3. Nonuniform grid used in the simulations.**

where $m$ is the number of grid points in the $\varphi$-direction. This distribution resulted in a sufficiently fine resolution in the wake region of the bubble. The parameters studied were the number of grid points as well as the distance of the outflow boundary from the bubble surface. For example, a $\lambda$-value of 10 corresponds to a grid where the outflow boundary in physical coordinates is at a distance of 10 times the smaller bubble semiaxis. The larger $\lambda$ becomes, the smaller is the impact of the outflow boundary condition on the bubble, but at the same time the resolution decreases. Table 2 gives the computed drag coefficients for two different grid sizes and $\lambda$ values. It can be seen that the error is less than 1% for $\lambda > 40$. The deviation from the predicted value is slightly higher for higher grid resolution. This might be due to the fact that the aspect ratio is not exactly unity, but 0.98.

Based on these results a grid of $n\times m = 60\times 60$ with a $\lambda$-value of 40 was chosen. The grid is shown in Figure 3 for $\delta = 0.5$. In Figure 4, a comparison between numerically predicted $C_d$-values and Eq. 31 is shown. Note that for Reynolds numbers higher than 40, the $C_d$ value is time-averaged due to the unsteady nature of vortex shedding. It can be seen that the computed values are very accurate. Also reattachment lengths and separation angles (not shown here) agree very

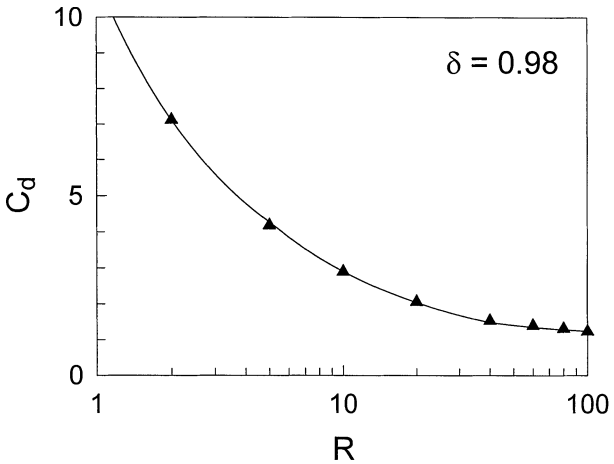


**Figure 4. Drag coefficients for the flow around a circular solid cylinder—, literature values; triangles, this study.**

well with data in the literature (Braza et al., 1986). Therefore, it can be concluded that the simulation code accurately predicts the flow close to a bluff body.

Conservation of mass (for components $A$, $B$, $R$, and $S$) was checked by integrating fluxes along several concentric shells in the integration domain. A maximum mass loss of $\pm 1\%$ was obtained in all simulations.

### *Vortex shedding*

In the case of a solid circular cylinder, vortex shedding occurs at Reynolds numbers of 40 and higher. In this regime, perturbations cannot be dampened and the resulting flow pattern shows asymmetric separation of vortices from the cylinder, which are transported away from the cylinder by convection and diffusion, forming the well-known Kármán vortex street. In Figure 5, the lift coefficient for the flow around a solid circular is shown at $R = 38$ and $R = 42$. It can be seen that for the lower Reynolds number, an initial perturbation is dampened and a stable recirculation pattern develops. However, for $R = 42$, stable asymmetric vortex shedding is obtained. Therefore, we can conclude that the numerical method used accurately predicts the onset of vortex shedding.

Vortex shedding has been observed in numerous experiments. In general, experimental conditions are never perfect. Nonuniform inlet conditions, irregular boundary conditions, vibrations, and other sources of disturbances can be expected, which are dampened below and amplified above $R = 40$. In the case of numerical simulations, however, disturbances are absent. It has been observed by several researchers that in numerical solutions—even for $R$-values significantly higher than 40—only symmetric recirculation and no vortex shedding is obtained. For example, numerical experiments with Reynolds numbers of 100 and 200 by Braza et al. (1986) showed that without initial perturbation, the flow always achieves a steady symmetric solution after a certain establishment period. A similar behavior can be expected for the simulation of flows past perfect-slip surfaces (bubbles). Therefore, in numerical simulations it is necessary to initially perturb the flow field in order to generate vortex shedding. A sinusoidal oscillating flow in the $y$-direction was chosen and initially superimposed to the flow in the $x$-direction, that is,

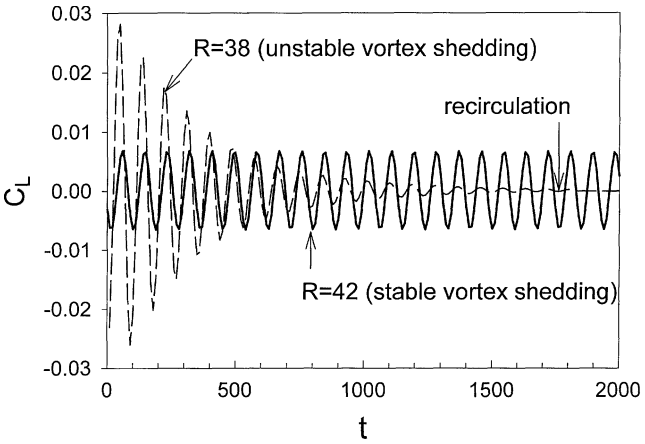


**Figure 5. Time evolution of the lift coefficient for the flow around a circular solid cylinder at $R = 38$ and $R = 42$.**

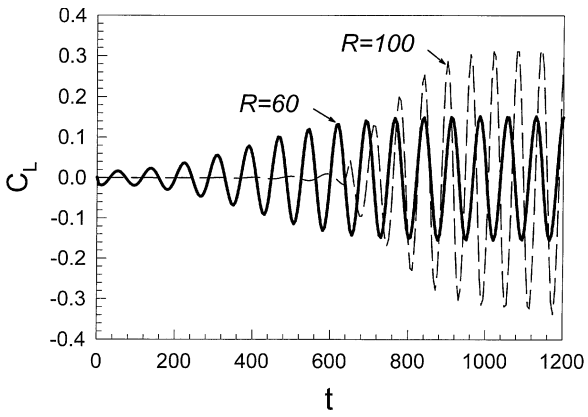


**Figure 6. Time evolution of the lift coefficient of an elliptical bubble ($\delta = 0.5$) at $R = 60$ and $R = 100$.**

For $R = 60$ the flow field was initially perturbed.

$$V_{in} = A \sin(Kt), \tag{33}$$

where $A$ is the amplitude (0.01), and $K$ was chosen to give a Strouhal number (see below) of approximately 0.2, that is, the typical dimensionless vortex shedding frequency. After vortex shedding was established, the periodic flow was stable without any need for numerical perturbation. For $R = 60$, perturbation of the flow field was necessary to generate vortex shedding. Thus, two stable states exist, at least numerically. For a Reynolds number of 100, however, vortex shedding occurred after a given amount of time without perturbing the flow. This can be seen in Figure 6, which shows the lift coefficient of an elliptical bubble ($\delta = 0.5$). In the case of $R = 60$, the flow was perturbed according to Eq. 33, while for $R = 100$ no perturbations were used. For both cases it can be seen that after some time a stable periodic state with constant amplitude (periodic vortex shedding) is obtained.

In the literature there exist a few studies on vortex shedding of 2-D gas bubbles, which are released in a narrow gap between two solid walls, called a "restricted two-dimensional" flow system (Fan and Tsuchiya, 1990). Vortex shedding was observed for Reynolds numbers as low as 42 (Rigby and Capes, 1970).

The Strouhal number is another indicator for the accuracy of the numerical solution. The Strouhal number is defined as the dimensionless frequeny of vortex shedding

$$St = \frac{fd_b}{U_\infty}. \tag{34}$$

In our computations the oscillations of the lift coefficient $C_1$ (solid cylinder) gave a value of $St = 0.167$ for $R = 100$, in agreement with many experimental (Tritton, 1959) and numerical results (Jordan and Fromm, 1972; Braza et al., 1986).

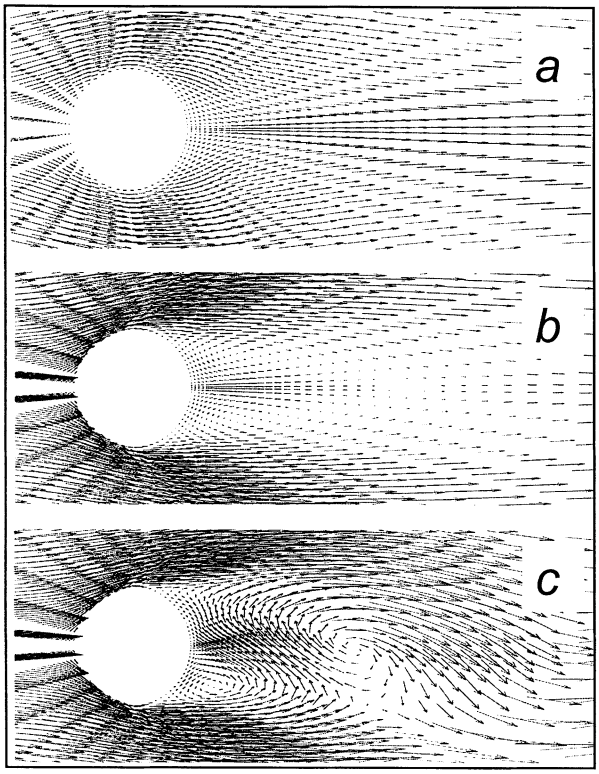


**Figure 7. Flow around a circular cylinder for: (a) $R = 1$, (b) $R = 30$, (c) $R = 100$.**

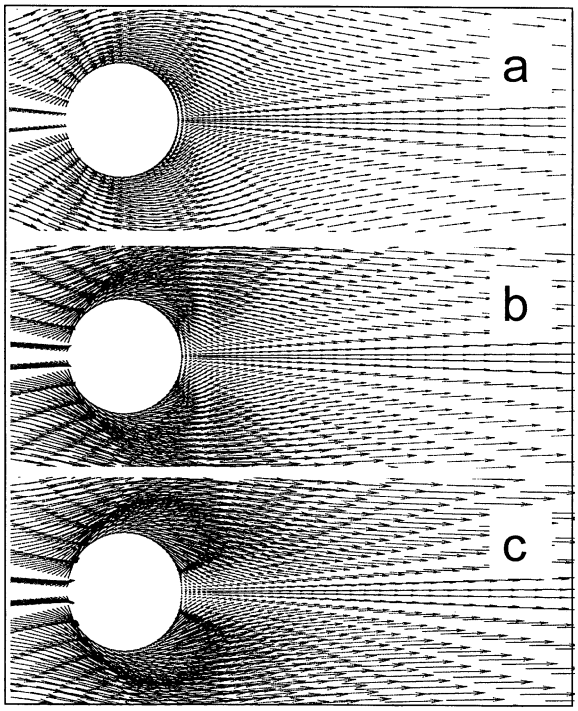


**Figure 8. Flow field around a circular bubble at: (a) $R = 1$, (b) $R = 20$ (c), $R = 100$.**

For lower $R$, $St$ are: 0.12 ($R = 50$); 0.139 ($R = 60$); 0.158 ($R = 80$). For higher Reynolds numbers, the Strouhal number approached 0.2 and remained more or less constant.

Finally, in Figure 7 the flow field around a solid circular cylinder at Reynolds numbers 1, 30, and 100 is shown, and it can be seen that for low $R$ a closed wake is obtained, for $R = 30$ recirculation occurs, and for $R = 100$ vortex shedding occurs. The obtained flow fields are very similar to the ones obtained by Braza et al. (1986), once again supporting the reliability of our solution procedure.

In summary, the exact predictions of drag coefficients, vortex shedding, reattachment lengths, and Strouhal number suggest that the numerical simulation code describes accurately the flow around bluff bodies. For the flow around a single bubble, only the no-slip boundary condition has to be replaced by the perfect-slip boundary conditions. Thus, the generated results can be expected to be accurate.

## Results and Discussion

### *Bubble hydrodynamics*

Circular bubbles do not create enough vorticity to cause recirculation and/or vortex shedding. In circular bubbles the surface vorticity $\omega_s$ is never sufficiently large—in the face of increasing convective vorticity transport away from the bubble with increasing Reynolds number—to produce recirculating wakes. As the bubble deforms, regions of sufficiently high curvature create enough vorticity, even though this mechanism is a smaller source of vorticity formation than the no-slip boundary condition. Since vorticity is not removed from the bubble at a sufficient rate, a recirculating wake or vortex shedding develops (Leal, 1989).

In Figure 8, the flow field around a circular bubble is shown for Reynolds numbers of 1, 20, and 100. It can be seen that no recirculating wake develops. Vortex shedding cannot be induced, no matter how large the perturbations that are chosen. Figure 9 shows the flow field around an elliptical bubble of aspect ratio $\delta = 0.5$. It can be seen that at $R = 1$ and 10 no recirculation exists. However, at $R = 20$, a recirculatory region is established, and for Reynolds numbers higher than 53 (Figure 9d), vortex shedding occurs. For an aspect ratio of $\delta = 0.25$, recirculation can be observed at Reynolds numbers as low as 5 due to the higher curvature, and vortex shedding is stable at Reynolds numbers above 25, as shown in Figure 10c.

### *Gas–liquid mass transfer*

Different flow regimes behind a bubble lead to different mass-transfer characteristics, which may influence the selectivity of competing reactions. This is illustrated in Figure 11, which shows the mass transport of the gaseous reactant $B$ into an inert liquid for a bubble of aspect ratio of 0.5. For $R = 5$, a region of high concentration of $B$ is formed in the bubble wake. In this case, no recirculatory wake exists. However, for $R = 20$, recirculation is established and the region of high $B$ concentration is clearly reduced, thus decreasing the selectivity of the reaction with higher reaction order with respect to $B$. The recirculatory region acts as an efficient micromixer and disperses $B$ quickly in the wake. A similar, even stronger, effect is obtained for $R = 60$ due to vortex shed-

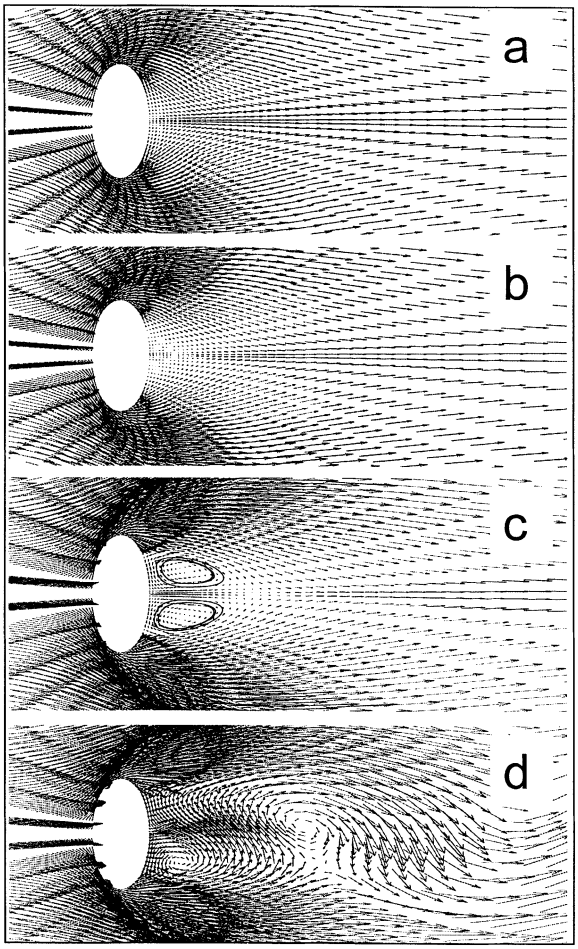


**Figure 9. Flow field around an elliptical bubble ($\delta = 0.5$): (a) $R = 1$, (b) $R = 10$, (c) $R = 20$, (d) $R = 60$.**

ding. Patches rich in the dissolved gas are formed and are convected away from the bubble. Thus, fast dispersion of $B$ in the liquid is obtained. However, there is a qualitative differene between recirculation and vortex shedding. It is evident that the residence time in a recirculatory wake is larger than the one for vortex shedding. If the residence times of the reactants in the wake are important, the selectivity of the two regimes may be quite different. Reactive-flow computations (see below) will illustrate this point.

In addition to improved mixing, the gas–liquid mass transfer is increased due to vortex shedding. In Figure 12, the integral Sherwood numbers for three bubble types are plotted vs. the Reynolds number for an inert solvent with a gaseous component $B$ dissolving in the liquid. The Sherwood number was computed according to

$$Sh = \frac{k_l d_1}{D_B} = \frac{1}{c_{B,\mathrm{eq}}} \frac{-\int_0^{2\pi} \left.\frac{\partial c_B}{\partial \eta}\right|_{\eta=\eta_0} d\varphi}{\int_0^{2\pi} h(\eta_0, \varphi)\, d\varphi}.$$

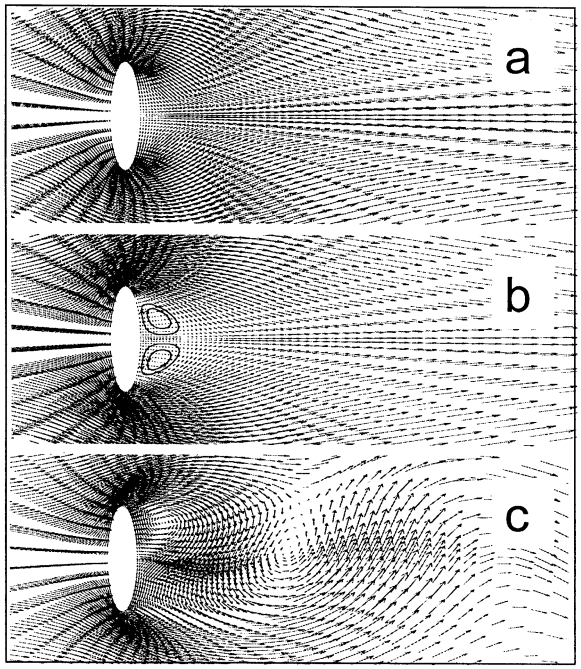


**Figure 10. Flow field around an elliptical bubble ($\delta = 0.25$): (a) $R = 1$, (b) $R = 5$, (c) $R = 40$.**

In Figure 12, we can see that for low Reynolds numbers, the Sherwood numbers are approximately equal. In fact, the Sherwood number of the elliptical bubbles is slightly smaller, which can be explained by the recirculating wake, which inhibits efficient removal of the gaseous reactant from the bubble rear. However, as soon as vortex shedding is induced, it can be observed that the Sherwood number becomes (slightly) larger than that of the circular bubble. Since it is well known that the bubble rear's contribution to the overall mass transfer is low, the increase is moderate and the differences between closed wakes and vortex shedding in terms of mass transfer is moderate. In fact, at a Reynolds number of 100, the Sherwood number of the bubble with $\delta = 0.25$ is increased by only 25% compared to a circular bubble. Comparison of the Sherwood number with correlations is the literature (Masliyah and Epstein, 1972; Carra and Morbidelli, 1986) shows a good match of our predictions and literature data. For example, the modified Boussinesq equation (Ponoth and McLaughlin, 2000) for a spherical inviscid gas bubble ($Sh = 1.13 \cdot (1 - 2.96/\sqrt{R})^{0.5}\sqrt{Pe}$) predicts for $R = 50$ (100) a Sherwood number of 19.3 (30.0), while our computations give a value of 17.5 (26.4). The difference between these values can be explained by the fact that the bubble in our computations is cylindrical and not spherical. (For example, Nusselt numbers for spheres are higher than for cylinders at the same Reynolds and Prandtl numbers).

### *Reaction selectivity*

The network investigated is a parallel-consecutive reaction network

$$R_1\colon A + B \rightarrow R, \quad R_2\colon R + B \rightarrow S. \tag{35}$$

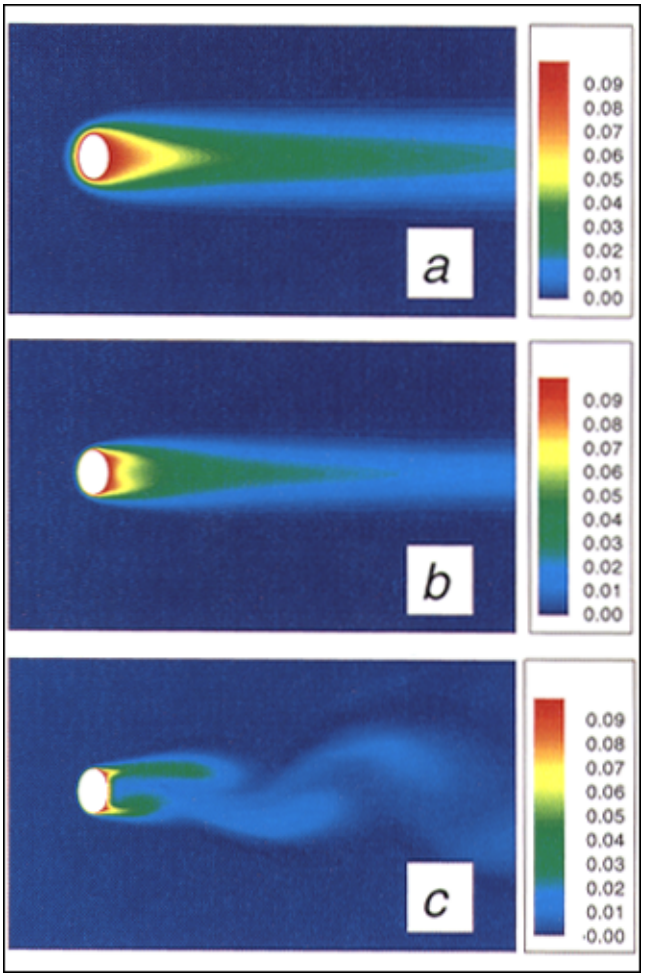


**Figure 11. Mass transport of a gaseous reactant *B* into an inert liquid for $\delta = 0.5$: (a) $R = 5$, (b) $R = 20$, (c) $R = 60$.**

Color code = dimensionless concentration of *B*.

The Damköhler number of the first reaction was chosen to be $Da_1 = 0.01$, 0.1 or 1, which corresponds to intermediate, fast, or very fast reactions. For $Da_1 = 0.01$, the conversion of the gaseous reactant at a distance of 20 times the minor semiaxis is between 30 and 60%, depending on the choice of $Da_2$. For $Da_1 = 0.1$, the conversions are betwen 95 and 99.5%, and for $Da_1 = 1$, conversions are larger than 99.99%. For each value of $Da_1$, different $Da_2$ values were chosen, such that $\kappa = Da_2/Da_1$ is equal to 1, 20, or 500. Selectivity toward products *R* and *S* are computed by

$$Y_R = \left.\frac{N_{R,\text{out}}}{N_{R,\text{out}} + N_{S,\text{out}}}\right|_{\eta = \eta_\infty}, \quad Y_S = 1 - Y_R. \tag{36}$$

$N_R$ and $N_S$ are the convective and diffusive fluxes of *R* and *S* across the external boundary of the integration domain.

In Figure 13, the selectivity toward the primary product *R* is shown for different Reynolds numbers and reaction parameters for a circular bubble, that is, a system where no recirculation and vortex shedding occurs. It can be seen that for the chosen reaction network, the selectivity strongly depends on

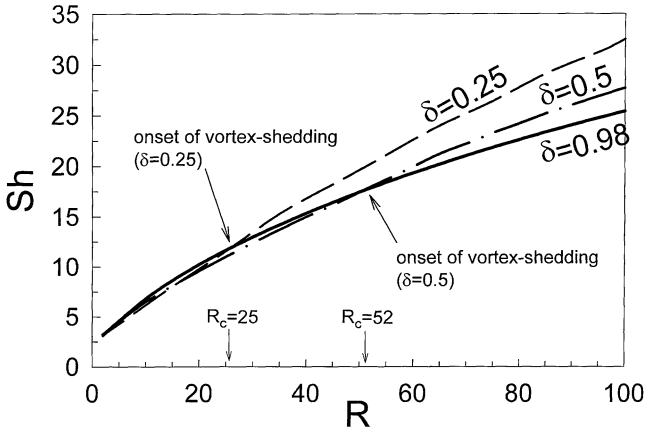


**Figure 12. Sherwood numbers for mass transport of a pure gaseous component into an inert liquid for a circular bubble ($\delta = 0.98$), and two elliptical bubbles ($\delta = 0.5$ and $\delta = 0.25$).**

Values above the onset of vortex shedding are time-averaged.

the system parameters. Clearly, the selectivity $Y_R$ decreases with increasing $\kappa$, which is expected, since the second reaction rate is higher at larger $\kappa$. However, the reaction selectivity increases with decreasing reaction rates (at constant relative rate contants $\kappa$) and increasing Reynolds numbers, which is not intuitive.

In order to explain these results, the concentration fields of all reactants (and the flow field) are shown in Figure 14 for $\kappa = 1$ and for two different $Da_1$ and *R* numbers. No color codes are provided, since the figure is used only for a qualitative interpretation of our results. However, color codes are identical in each column (within each species). For a Reynolds number of 5 and $Da_1 = 0.01$, the concentration of *A* is approximately uniform, since the reaction rates are relatively small. The concentration of *B* in the wake is high, *B* reacts preferentially with *A* at a low rate, and the formation rate of *S* is very low (concentration of *R* is low), thus explaining the high selectivity of 98.3%. In the case of a very fast reaction ($Da_1 = 1$), however, the situation is very different. In this case, the gaseous reactant *B* is consumed very close to the bubble. At the same time, *A* is depleted in the wake of the bubble due to the very high reaction rates and due to the insufficient

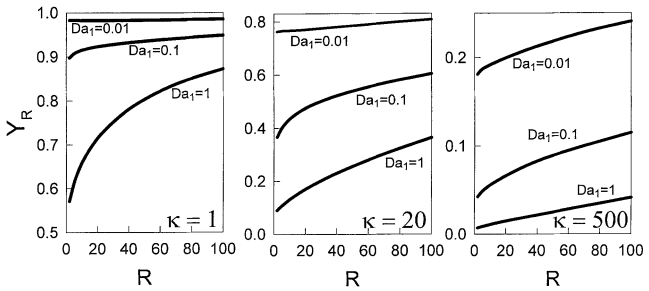


**Figure 13. Selectivity toward the primary product *R*, $Y_R$, for a circular bubble as a function of Reynolds number, $Da_1$, and $\kappa$.**

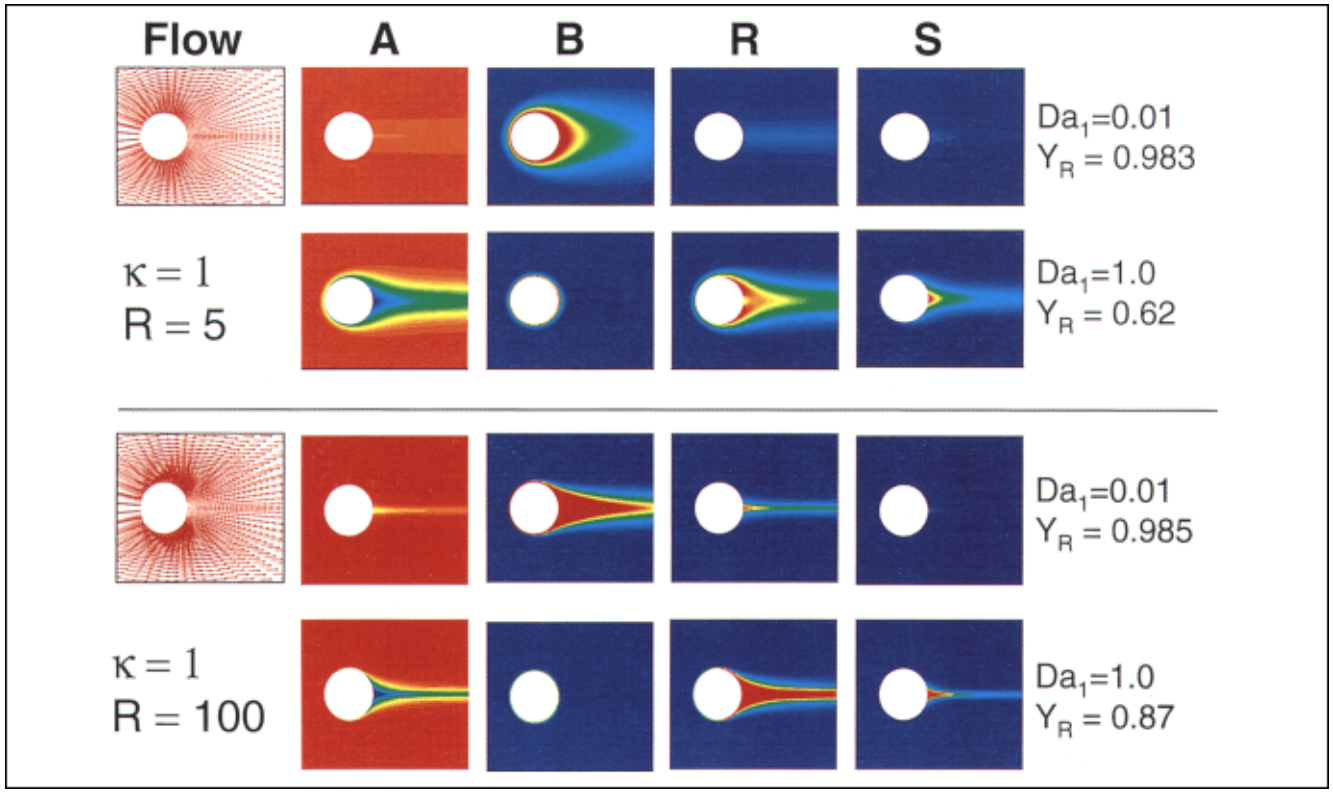


**Figure 14. Flow field and concentrations of components *A*, *B*, *R*, and *S* for a circular bubble.**

The color codes in each column are identical.

supply of fresh reactant (residence time in the wake is higher). Thus, a region in the bubble wake is created, which is low in $A$, rich in $B$, and the product $R$ (which is formed close to the bubble surface). These effects increase the reaction rate of the second reaction (see the concentration field of $S$), and thus lead to a significantly reduced selectivity of 62%. Comparing only the results of $Da_1 = 1$, the concentration fields at $R = 100$ look similar to the ones at $R = 5$, but it can be seen that the "concentration wake" is significantly smaller, which is due to the larger impact of convection compared to diffusion ($Pe = Sc \cdot \hat{R}$). Therefore, the region in the bubble wake, in which $A$ is depleted, is significantly smaller. The lowest dimensionless concentration of $A$ in the bubble wake is 0.15 for $R = 5$, while it is 0.25 for $R = 100$ (for $Da_1 = 1$). These combined effects lead to a significantly reduced secondary product formation, and thus the selectivity increases to 87% vs. 62% for $R = 5$. This also can be seen in Figure 15, which shows the formation rate of component $R$. Obviously, the reaction rate of $R$ is very small in the bubble wake, but the region of low formation rate is smaller at higher Reynolds number. Note, that the grid used in our computation can resolve the very thin reaction layer.

In Figure 16, the selectivity toward the product $R$ for an elliptical bubble of $\delta = 0.5$ is shown. Although the overall trend is similar to a circular bubble (such as $Y_R$ decreases with increasing $\kappa$ and with increasing $Da_1$) there are obvious

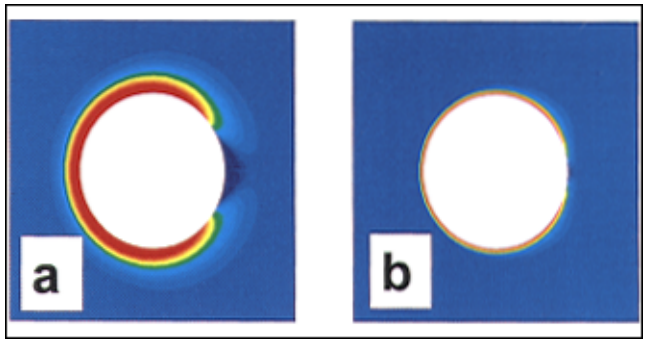


**Figure 15. Formation rate of product *R* for a circular bubble for $Da_1 = 1$ and $\kappa = 1$; (a) $R = 5$, (b) $R = 100$.**

Color codes in both figures are identical.

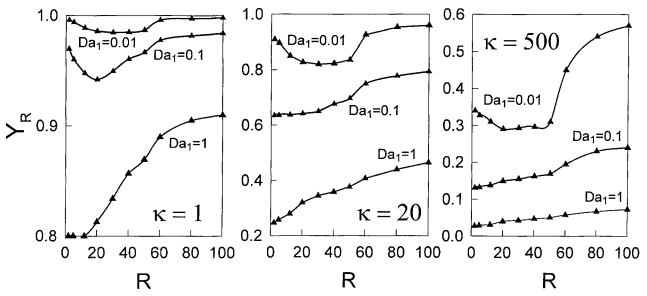


**Figure 16. Selectivity $Y_R$ toward the primary product *R* for an elliptical bubble ($\delta = 0.5$) as a function of Reynolds number, $Da_1$, and $\kappa$.**

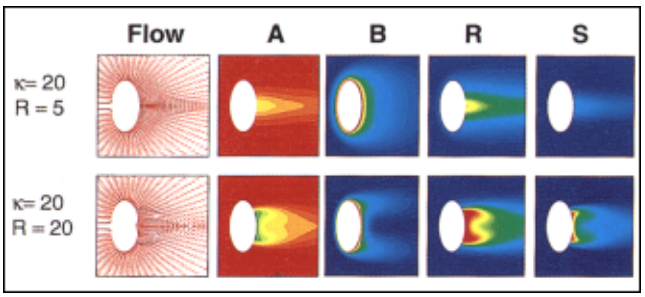


**Figure 17. Flow field and concentrations of components *A*, *B*, *R*, and *S* for an elliptical bubble ($\delta = 0.5$); the color codes in each column are identical.**

Velocity vectors have uniform length.

differences. The main differences are (1) the selectivity toward $R$ is 10–15% higher for the elliptical bubble at the same Reynolds number, and (2) most importantly, the selectivity initially decreases with the Reynolds number. At a critical $R$, however, the selectivity increases sharply (except for very fast reactions).

The first effect is due to the smaller surface area of an elliptical bubble leading to a lower overall conversion of $A$ and $B$ close to the bubble. (For a given Reynolds number the maximum diameter of the circular and the one of the elliptical bubble are the same. Therefore, the elliptical bubble has a smaller surface area.) Levels of $A$ and $B$ are higher in the wake, leading to a larger selectivity toward the primary product. The second finding can be explained by the different wake dynamics in the case of the elliptical bubble. The initial decrease of $Y_R$ coincides with the onset of recirculation. Recirculation causes a significantly longer residence time in the bubble wake, leading to an overall lower concentration of the reactant $A$ in the wake. This can be seen in Figure 17 ($Da_1 = 0.01$), which compares the flow and concentration fields

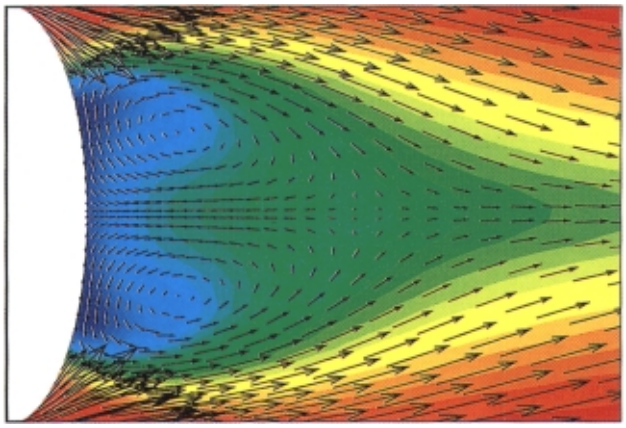

**Figure 18. Concentration field of component *A* and recirculatory flow in the bubble wake for an elliptical bubble ($\delta = 0.5$); $R = 20$, $Da_1 = 0.01$, $\kappa = 20$.**

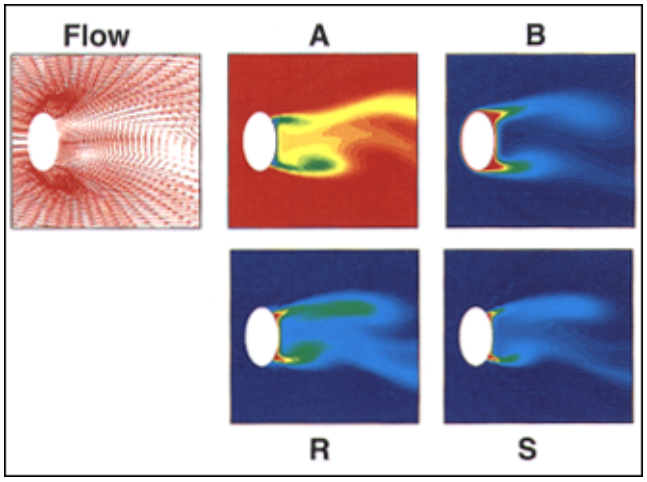


**Figure 19. Snapshot of the flow and concentration fields of components *A*, *B*, *R*, and *S* for an elliptical bubble ($\delta = 0.5$); $R = 60$, $Da_1 = 0.1$, $\kappa = 1$.**

for $R = 5$ and $R = 20$. At $R = 20$, fresh reactant $B$ is transported into the wake from the bubble's rear interface, but transport of the liquid reactant $A$ into the wake is severely limited by the recirculating pattern. Effectively, the recirculating pattern in the wake acts as a transport barrier for $A$. Thus, since the concentration of $A$ is low, a larger fraction of the reactant $B$ reacts with $R$ to form the secondary product, leading to a decrease of the selectivity. The effective reduction of transport of $A$ into the wake is illustrated in Figure 18, which shows the concentration of $A$ and the flow field in the bubble wake. It can be seen that the liquid rich in $A$ is flowing past the bubble without entering the bubble wake. Additionally, close to the bubble rear surface, the recirculation in the direction of the bubble edge prevents flow of the bulk liquid into the region close to the bubble interface. For very fast reactions ($Da_1 = 0.1$ and large $\kappa$, and for all cases with $Da_1 = 1$), however, the reaction zone is so small that wake recirculation doesn't impact the reaction. Therefore, the decrease in selectivity is small and cannot be observed in Figure 16.

Vortex shedding occurs at Reynolds numbers higher than 52, which causes a sudden increase in selectivity (see Figure 16). Once vortex shedding occurs, patches of the dissolved reactant $B$ are quickly convected away from the bubble into regions rich in $A$, thus leading to significantly higher selectivities toward $R$. This can be seen in Figure 19, which shows a snapshot of the concentration fields of reactants $A$ and $B$, and of the products $R$ and $S$. In effect, the transition from a closed wake to an open wake qualitatively changes the mixing behavior, which can lead to a large change in the reaction selectivity. Again, for very fast reactions this effect is negligible, since most of the gaseous reactant is consumed very close to the bubble, and the wake region effectively does not participate in the reaction.

Other reaction networks were investigated in this study. For example, for the parallel-competitive reaction network

$$R_1\colon A + B \rightarrow R \quad \text{and} \quad R_2\colon A + 2B \rightarrow S, \qquad (37)$$

with dimensionless reaction rates

$$r_1 = Da_1 \cdot c_A \cdot c_B, \quad r_2 = Da_2 \cdot c_A \cdot c_B^2, \tag{38}$$

the effect of vortex shedding on the selectivity was small, mainly because both reactions were linear in $A$.

## Summary

In this study the impact of 2-D bubble dynamics on the selectivity of fast gas–liquid reactions was investigated. Although it is known that different bubble shapes and sizes create different local mixing characteristics—by recirculation, vortex shedding, or the lack of thereof—these issues have not been addressed in the reaction engineering literature. In this study the reactive flow around a single bubble was investigated using a 2-D reaction model of a single bubble. A parallel-consecutive reaction network with different reaction rates was investigated.

Several simplifications were introduced. For example, it was assumed that the bubble has a constant shape (no shape fluctuations) and a stationary position with respect to the main flow direction, that is, the effects of vortex shedding on the bubble path were neglected. Additionally, only circular and elliptical bubbles were considered. The primary justification for this simplification is that the main qualitative differences can be expected to occur between cases where no recirculation and/or vortex shedding occurs (circular bubbles) and cases were recirculation or vortex shedding is obtained (elliptical, circular cap, elliptical cap). The study presented is a qualitative analysis of the processes close to a single bubble. Effects like 3-D vortex shedding, bubble–bubble interactions, liquid-phase turbulence, and catalyst suspension have to be investigated in further studies. The main results of our work can be summarized as follows:

- The increased residence time in the wake region can cause the formation of different products than those formed at the bubble roof.
- Recirculation in the bubble wake increases locally the residence time and acts as a transport barrier for the liquid-phase reactants but not for the gaseous reactant. Thus, depletion of the liquid-phase reactant in the bubble wake can lead to an increase or decrease in the byproduct formation if both reactions are competing for the gaseous reactant, but their reaction rates are not linear with respect to the liquid-phase concentration.
- Vortex shedding causes a qualitatively different mixing environment, since patches rich in the dissolved gas are quickly convected away from the bubble into regions with a high concentration of the liquid reactant.
- In the case of extremely fast reactions, bubble-wake dynamics do not impact the product distribution, since the reaction is completed in a very thin layer close to the interface. In this case, the wake region does not participate in the reaction.

In summary, it can be seen that size and shape of bubbles in the bubbly flow regime can significantly increase or lower the selectivity toward the desired product. Since bubbles shapes and sizes (and the resulting bubble dynamics) can be controlled by changing operating conditions (gas feed rate, liquid viscosity, surface tension, and so on) or design parameters (sparger design, nozzle sizes, and so on) the selectivity of fast gas–liquid reactions can be controlled.

Although the presented study addresses only a generic reaction system, the presented methodology can be applied to actual reaction systems in order to enable a rational design, control, scale-up, and optimization of existing or new processes. Furthermore, this study can help explain inconsistencies that were observed during scale-up of existing processes. Even though this work addresses only bubble columns, it may have relevance for stirred systems. While bubble flow in stirred systems is significantly more complex than in bubble columns, the impact of single-bubble dynamics in stirred tanks may be similar and has to be studied.

Further work will be needed to extend the presented work to the reactor level, which is difficult due to the lack of understanding of the flow on the reactor scale. Reliable model reduction techniques and multiscale modeling approaches will be necessary for this task. Bubble interactions, like coalescence and breakup, as well as liquid-phase turbulence have to be included in the present analysis to obtain results that apply to bubble column operating in the churn-turbulent flow regime.

## Acknowledgment

This work was partially supported by a DuPont Young Professor Award.

## Notation

$a$ = half the interfocal distance of the ellipse, m
$AR$ = grid aspect ratio
$d_b$ = diameter of a volume-equivalent sphere, m
$d_{1(2)}$ = major (minor) semiaxis of the ellipse, m
$c_{A,In}$ = bulk concentration of component $A$, kmol/m$^3$
$\hat{c}_i$ = concentration of component $i$, kmol/m$^3$
$c_i$ = dimensionless concentration of component $i$
$C_d$ = drag coefficient
$C_l$ = lift coefficient
$D$ = diffusion constant in the liquid phase, m$^2$/s
$Da$ = Damköhler number, $a \cdot k \cdot c_{A,In}/U_\infty$
$Eo$ = Eötvös number, $= g \rho_l d_b^2/\sigma$
$f$ = vortex shedding frequency, 1/s
$\boldsymbol{g}$ = metric transformation tensor, m$^2$
$h$ = dimensionless scale factor
$H$ = scale factor, m
$k$ = reaction-rate constant, m$^3$/kmol/s
$k_l$ = liquid-side mass-transfer coefficient, m/s
$n$ = number of grid points in $\eta$-direction
$m$ = number of grid points in $\varphi$-direction
$Mo$ = Morton number, $= g \mu_l^4/(\rho_l \cdot \sigma^3)$
$\hat{P}$ = pressure, Pa
$P$ = dimesionless pressure
$Pe$ = Peclet number, $= U_\infty a/D$
$r$ = dimensionless reaction rate
$\hat{R}$ = Reynolds number based on $a$, $= aU_\infty \rho/\mu$
$R$ = Reynolds number, $= d_1 U_\infty \rho/\mu$
$R_b$ = bubble Reynolds number based on equivalent sphere diameter, $= d_b U_\infty \rho/\mu$
$Sc$ = Schmidt number, $= \mu/(\rho \cdot D)$
$Sh$ = Sherwood number, $= k_l \cdot d_1/D$
$St$ = Strouhal number, $= f d_b/U_\infty$
$\hat{t}$ = time, s
$t$ = dimensionless time
$\hat{u}$ = velocity in $\eta$-direction, m/s
$u$ = dimensionless velocity in $\eta$-direction
$U_{in}$ = terminal bubble rise velocity, m/s
$\hat{v}$ = velocity in $\varphi$-direction, m/s
$v$ = dimensionless velocity in $\varphi$-direction

$V_{in}$ = perturbation velocity in $y$-direction, m/s
$We$ = Weber number, $= \rho_l U_\infty^2 d_b/\sigma$
$x$ = physical $x$-coordinate, m
$y$ = physical $y$-coordinate, m
$Y$ = selectivity

### Greek letters

$\alpha$ = grid angle
$\delta$ = aspect ratio $d_2/d_1$
$\epsilon$ = relative error of solver
$\eta$ = transformed coordinate direction
$\gamma$ = up-winding factor
$\varphi$ = transformed coordinate direction
$\kappa$ = ratio of Damköhler numbers, $Da_2/Da_1$
$\mu$ = liquid viscosity, Pa·s
$\nu_{ij}$ = stoichiometric coefficient of reactant $i$ in reaction $j$
$\rho$ = liquid density, kg/m$^3$
$\sigma$ = surface tension, N/m
$\hat{\tau}$ = stress tensor, N/m$^2$
$\tau$ = dimensionless stress sensor
$\hat{\omega}$ = vorticity, l/s
$\omega$ = dimensionless vorticity

### Indices

eq = equilibrium at the gas/liquid interface
$in$ = bulk concentration
$s$ = bubble surface

## Literature Cited


Arters, D. C., and L. S. Fan, "Experimental Methods and Correlation of Solid-Liquid Mass Transfer in Fluidized Beds," *Chem. Eng. Sci.*, **45**, 965 (1990).

Baird, H. I., and J. F. Davidson, "Gas Absorption by Rising Large Bubbles," *Chem. Eng. Sci.*, **17**, 5109 (1962).

Baldyga, J., and J. R. Bourne, *Turbulent Mixing and Chemical Reactions*, Wiley, New York (1999).

Beenackers, A. A. C. M., and W. P. H. van Swaaij, "Chemical Reactor Design and Technology," *Washington Nato Advanced Study Institute Series*, H. I. DeLasa, ed., Martinus Nijhoff, p. 463 (1986).

Bhaga, D., and M. E. Weber, "Bubbles in Viscous Liquids: Wakes, Shapes and Velocities," *J. Fluid Mech.*, **105**, 61 (1981).

Bourne, J. R., E. Crivelli, and P. Rys, "Mixing-Disguised Azo Coupling Reactions," *Helv. Chim. Acta*, **60**, 2944 (1977).

Braza, M., P. Chassaing, and H. Ha Minh, "Numerical Study and Physical Analysis of the Pressure and Velocity Field in the Near Wake of a Circular Cylinder," *J. Fluid Mech.*, **165**, 79 (1986).

Brenan, K. E., S. L. Campbell, and L. R. Petzold, *Numerical Solution of Initial-Value Problems in Differential-Algebraic Equations*, Society for Industrial and Applied Mathematics, Philadelphia (1995).

Brignell, A. S., "Mass Transfer from Spherical Cap Bubbles in Laminar Flow," *Chem. Eng. Sci.*, **29**, 135 (1974).

Calderbank, P. H., D. S. L. Johnson, and J. London, "Mechanics and Mass Transfer of Single Bubbles in Free Rise Through Some Newtonian and Non-Newtonian Liquids," *Chem. Eng. Sci.*, **25**, 235 (1970).

Carra, S., and M. Morbidelli, "Transient Mass Transfer onto Small Particles and Drops," *Handbook of Heat and Mass Transfer*, Vol. 2, P. Cheremisinoff, ed., Gulf Publishing, Houston (1986).

Chowdhry, S., and A. A. Linninger, "Computer Aided Formulation and Analysis of Dynamic Systems," AIChE Meeting, Dallas, TX (1999).

Clift, R., J. R. Grace, and M. E. Weber, *Bubbles, Drops and Particles*, Academic Press, New York (1978).

Coppus, J. H. C., and K. Rietema, "Theoretical Deviation of the Mass Transfer Coefficient at the Front of a Spherical Cap Bubble," *Chem. Eng. Sci.*, **35**, 1497 (1980).

Coppus, J. H. C., and K. Rietema, "Mass Transfer from Spherical Cap Bubbles, the Contribution of the Bubble Rear," *Trans. Inst. Chem. Engrs.*, **59**, 54 (1981).

Danckwerts, P. V., "The Effect of Incomplete Mixing on Homogeneous Reactions," *Chem. Eng. Sci.*, **8**, 93 (1958).

David, R., and J. Villermaux, "Interpretation of Micromixing Effects on Fast Consecutive Competing Reactions in Semi-Batch Stirred Tanks by a Simple Interaction Model," *Chem. Eng. Commun.*, **54**, 333 (1987).

Deuflhard, P., E. Hairer, and J. Zugck, "One-Step and Extrapolation Methods for Differential-Algebraic Systems," *Numer. Math.*, **51**, 1 (1987).

Doraiswamy, L. K., and M. M. Sharma, *Heterogeneous Reactions*, Vol. 2, *Fluid-Fluid-Solid Reactions*, Wiley, New York (1984).

Ehrig, R., U. Nowak, L. Oeverdieck, and P. Deuflhard, "Advanced Extrapolation Methods for Large-Scale Differential Algebraic Problems," *High-Performance Scientific and Engineering Computing*, H.-J. Bungartz, F. Durst, and C. Zenger, eds., Vol. 8, Springer, New York, p. 233 (1999).

Epstein, I. R., "The Consequences of Imperfect Mixing on Autocatalytic Chemical and Biological Systems," *Nature*, **374**, 231 (1995).

Fan, L. S., *Gas-Liquid-Solid Fluidization Engineering*, Butterworth-Heinemann, Boston (1989).

Fan, L.-S., and K. Tsuchiya, *Bubble Wake Dynamics in Liquids and Liquid-Solid Suspensions*, Butterworth-Heinemann, Boston (1990).

Fletcher, C. A. J., *Computational Techniques for Fluid Dynamics*, Springer, New York (1997).

Fox, R. O., "On the Relationship Between Lagrangian Micromixing Models and Computational Fluid Dynamics," *Chem. Eng. Process*, **37**, 521 (1998).

Froncioni, A. M., F. J. Muzzio, R. L. Peskin, and P. D. Swanson, "Chaotic Motion of Fluid and Solid Particles in Plane Wakes," *Chaos Solitons Fractals*, **8**(1), 109 (1997).

Gianetto, A., and O. L. Silveston, *Multiphase Chemical Reactors*, Hemisphere, Washington, DC (1986).

Grace, J. R., T. Wairegi, and T. H. Nguyen, "Shapes and Sizes of Bubbles Rising in Infinite Liquids," *Trans. Inst. Chem. Eng.*, **54**, 167 (1976).

Haberman, W. L., and R. K. Morton, *David K. Taylor Model Basin Report 802*, Navy Dept., Washington, DC (1953).

Hills, J. H., "The Two-Dimensional Elliptical Cap Bubble," *J. Fluid Mech.*, **68**, 503 (1975).

Hyndman, C., F. Larachi, and C. Guy, "Understanding Gas-Phase Hydrodynamics in Bubble Columns: A Convective Model Based on Kinetic Theory," *Chem. Eng. Sci.*, **52**, 63 (1997).

Jean, R. H., and L.-S. Fan, "Rise Velocity and Gas-Liquid Mass Transfer of a Single Large Bubble in Liquids and Liquid-Solid Fluidized Beds," *Chem. Eng. Sci.*, **45**, 1057 (1990).

Jordan, S. K., and J. E. Fromm, "Oscillatory Drag, Lift and Torque on a Circular Cylinder in a Uniform Flow," *Phys. Fluids*, **8**, 371 (1972).

Kleinman, L. S., and X. B. Reed Jr., "Interphase Mass Transfer from Bubbles, Drops, and Solid Spheres: Diffusional Transport Enhanced by External Chemical Reaction," *Ind. Eng. Chem. Res.*, **35**, 3621 (1995).

Khinast, J., D. Luss, T. M. Leib, and M. P. Harold, "Impact of an Undesired Reaction on a Boiling Slurry Reactor," *Chem. Eng. Sci.*, **54**, 2295 (1999a).

Khinast, J., D. Luss, T. M. Leib, and M. P. Harold, "The Adiabatic Boiling Slurry Reactor: Influence of Axial Dispersion," *Chem. Eng. Sci.*, **54**, 5021 (1999b).

Kondepudi, D. K., K. L. Bullock, J. A. Digits, and P. D. Yarborough, "Stirring Rate as a Critical Parameter in Chiral Symmetry Breaking Crystallization," *J. Am. Chem. Soc.*, **117**, 401 (1995).

Kramers, H., "Physical Factors in Chemical Reaction Engineering," *Chem. Eng. Sci.*, **8**, 45 (1958).

Krishna, R., and J. Ellenberger, "A Unified Approach to the Scale-Up of 'Fluidized' Multiphase Reactors," *Trans. Inst. Chem. Eng.*, **73**(A), 217 (1995).

Krishna, R., M. I. Urseanu, J. M. Van Baten, and J. Ellenberg, "Influence of Scale on the Hydrodynamics of Bubble Columns Operating in the Churn-Turbulent Regime: Experiments vs. Eulerian Simulations," *Chem. Eng. Sci.*, **54**, 4903 (1999).

Leal, L. G., "Vorticity Transport and Wake Structure for Bluff Bodies at Finite Reynolds Numbers," *Phys. Fluids A*, **1**, 124 (1989).

Lin, T.-J., J. Reese, T. Hong, and L. S. Fan, "Quantitative Analysis and Computation of Two-Dimensional Bubble Columns," *AIChE J.*, **42**, 301 (1996).

Lindt, J. T., "Note on the Wake Behind a Two-Dimensional Bubble," *Chem. Eng. Sci.*, **26**, 1776 (1971).
Lindt, J. T., "On the Periodic Nature of the Drag on a Rising Bubble," *Chem. Eng. Sci.*, **27**, 1775 (1972).
Long, W. M., and L. V. Kalachev, "On Dissolution of a Spherical Gas Bubble in the Presence of Fast Reaction," *Chem. Eng. Sci.*, **55**, 2295 (2000).
Masliyah, J. H., and N. Epstein, "Numerical Solution of Heat and Mass Transfer from Spheroids in Steady and Axisymmetric Flow," *Proc. Int. Symp. on Two-Phase Systems*, Pergamon Press, New York (1972).
Mills, P. L., and R. V. Chaudhari, "Reaction Engineering of Emerging Oxidation Processes," *Catal. Today*, **48**, 17 (1999).
Miyahara, T., K. Tsuchiya, and L.-S. Fan, "Wake Properties of a Single Gas Bubble in a Three-Dimensional Liquid-Solid Fluidized Bed," *Int. J. Multiphase Flow*, **14**, 749 (1988).
Moore, D. W., PhD Thesis, Univ. of Cambridge, Cambridge, UK (1958).
Mudde, R., D. Lee, and L. S. Fan, "Role of Coherent Structures on Reynolds Stresses in a 2-D Bubble Column," *AIChE J.*, **43**, 913 (1997a).
Mudde, R. F., J. Groen, and H. Van Den Akker, "Liquid Velocity Field in a Bubble Column: LDA Experiments," *Chem. Eng. Sci.*, **52**, 4217 (1997b).
Nienow, A. W., S. M. Drain, A. P. Boyes, R. Mann, A. M. El-Hamouz, and H. J. Carpenter, "A New Pair of Reactions to Characterize Imperfect Macromixing and Partial Segregation in a Stirred Semi-Batch Reactor," *Chem. Eng. Sci.*, **47**, 2825 (1992).
Noh, W. F., and P. Woordward, "SLIC (Simplified Line Interface Calculation," in *Lecture Notes in Physics*, A. I. van Dooren and P. J. Zandbergen, eds., Vol. 59, Springer, New York, p. 330 (1976).
Nyugen-Tien, K., A. N. Patwari, A. Schumpe, and W.-D. Decker, "Chemical Selectivities Disguised by Mass Diffusion," *AIChE J.*, **31**, 194 (1985).
Panton, R. L., *Incompressible Flow*, Wiley, New York (1996).
Paul, E. L., and R. E. Treybal, "Mixing and Product Distribution for a Liquid Phase, Second Order, Competitive-Consecutive Reaction," *AIChE J.*, **17**, 718 (1971).
Ponoth, S. S., and J. B. McLaughlin, "Numerical Simulation of Mass Transfer for Bubbles in Water," *Chem. Eng. Sci.*, **55**, 1237 (2000).
Pruppacher, H. R., B. P. LeClaire, and A. E. Hamielec, "Some Relations between Drag and Flow Pattern of Viscous Flow Past a Sphere and a Cylinder at Low and Intermediate Reynolds Number," *J. Fluid Mech.*, **44**, 781 (1970).
Ramachandran, P. A., and R. V. Chaudhari, *Three Phase Catalytic Reactors*, Gordon & Breach, New York (1983).
Reese, J., and L.-S. Fan, *Chem. Eng. Sci.*, **52**, 1553 (1997).
Rigby, G. R., and C. E. Capes, "Bed Expansion and Bubble Wakes in Three-Phase Fluidization," *Can. J. Chem. Eng.*, **48**, 19 (1984).
Ryskin, G. R., and L. G. Leal, "Numerical Solution of Free-Boundary Problems in Fluid-Mechanics, Part 1. The Finite Difference Technique," *J. Fluid Mech.*, **148**, 1 (1984a).
Ryskin, G. R., and L. G. Leal, "Numerical Solution of Free-Boundary Problems in Fluid-Mechanics, Part 2. Buoyancy Driven Motion of a Gas Bubble Through a Quiescent Liquid," *J. Fluid Mech.*, **148**, 19 (1984b).
Saffman, P. G., "Viscous Fingering in Hele-Shaw Cells," *J. Fluid Mech.*, **173**, 73 (1986).
Shah, Y. T., *Gas-Liquid-Solid Reactor Design*, McGraw-Hill, New York (1979).
Song, G.-H., and L.-S. Fan, "Gas-Liquid Mass Transfer of a Single Large Bubble in Liquids and Liquid-Solid Fluidized Beds," *AIChE J.*, **36**, 439 (1990).
Sun, Y., R. N. Landau, J. Wang, C. LeBlond, and D. G. Blackmond, "Asymmetric Hydrogenation of Ethyl Pyruvate: Diffusion Effects on Enantioselectivity," *J. Amer. Chem. Soc.*, **118**, 1348 (1996).
Sun, Y., J. Wang, C. LeBlond, R. A. Reamer, J. Laquidara, J. R. Sowa, Jr., and D. Blackmond," Kinetic Influences on Enantioselectivity in Asymmetric Catalytic Hydrogenation," *J. of Organmetall. Chem.*, 548, 65 (1997).
Sundaresan, S., "Modeling the Hydrodynamics of Multiphase Flow Reactors: Current Status and Challenges," *AIChE J.*, **46**, 1102 (2000).
Tannehill, J. C., D. A. Anderson, and R. H. Pletcher, *Computational Fluidmechanics and Heat Transfer*, Taylor and Francis, Washington, (1997).
Tritton, D. J., "A Note on Vortex Streets Behind Circular Cylinders at Low Reynolds Numbers," *J. Fluid Mech.*, **45**, 203 (1971).
van Krevelen, D. W., "Micro- and Macro-Kinetics," *Chem. Eng. Sci.*, **8**, 5 (1958).
Villermaux, J., L. Falk, M. C. Fournier, and C. Detrez, "Use of Parallel-Competing Reactions to Characterize Micromixing Efficiency," *AIChE Symp. Ser.*, Vol. 90, No. 299 (1992).
Villermaux, J., and L. Falk, "A Generalized Mixing Model for Initial Contacting of Reactive Fluids," *Chem. Eng. Sci.*, **49**, 5127 (1994).
Weber, M. E., "The Effect of Surface Active Agents on Mass Transfer from Spherical Cap Bubbles," *Chem. Eng. Sci.*, **30**, 1507 (1975).
Wu, T. Y., "Inviscid Cavity and Wake Flows," *Basic Developments in Fluid Dynamics*, M. Holt, ed. Academic Press, New York (1968).
Yabe, K., and D. Kunii, "Dispersion of Molecules Diffusing from a Gas Bubble into a Liquid," *Inst. Chem. Eng.*, **18**, 666 (1978).

*Manuscript received Nov. 28, 2000, and revision received Apr. 17, 2001.*